Journal of Applied Mechanics. Received November 30, 2024;
Accepted manuscript posted January 9, 2025. doi:10.1115/1.4067595

Rational design of low fatigue phase-transforming Cu-based alloys

Mostafa Karami[a,b], Xian Chen[b,*]

[a] *Department of Materials Science and Engineering, Sharif University of Technology, Tehran, Iran*
[b] *Department of Mechanical and Aerospace Engineering, Hong Kong University of Science and Technology, Hong Kong*

Abstract

In this study, we introduce a novel material descriptor and corresponding mechanical criteria to guide the development of low-fatigue shape memory alloys. Our approach synergistically combines compatibility theories, crystallographic algorithms, and micromechanical experiments to optimize materials through a two-parameter compositional tuning strategy. We demonstrate this method on a series of $CuAlx_1Mnx_2$ alloys, where the atomic composition vector $\mathbf{x} = (x_1, x_2) \in [0.17, 0.22] \times [0.09, 0.11]$. By employing a scalar-valued function to index the functional fatigue property based on cofactor conditions, we analyze the continuity and extremes with respect to compositional variables. Through just three iterative development steps, we identify the composition $CuAl_{20.2}Mn_{11.3}$, achieving a reduction in thermal hysteresis by a factor of 2 and enhancing mechanical reversibility up to 1000 cycles. This result underscores the potential of mathematical methods in designing complex materials with desirable mechanical properties. Our findings not only provide a theoretical framework for the design of shape memory alloys but also highlight the importance of integrating theoretical and experimental techniques to achieve optimal material properties.

Keywords: Martensitic microstructure, Shape memory alloys, Material descriptor, Compatibility

1. Introduction

Given the multidisciplinary nature of materials science, researchers across various fields strive to understand and design new materials with exceptional properties. Traditionally, the discovery of new materials has relied on a trial-and-error design cycle. Engineering heuristics has guided this discovery process for decades. However, transitioning a material from its initial discovery to an optimized state for practical use often takes more than a decade. For instance, the discovery of the magnetocaloric effect in magnetic materials [1] revolutionized modern refrigeration, and the discovery of the photovoltaic effect in semiconductors [2] transformed power generation technologies. Despite these groundbreaking discoveries, physicists and chemists have spent over a century improving the performance of these "novel" materials. Experimental

*Corresponding author
Email address: xianchen@ust.hk (Xian Chen)

property optimization is significantly more time-consuming than the optimization of software, algorithms, and simulation models.

Consider the example of shape memory alloys used in medical devices, energy damping, and smart actuators. Conventional material design strategies are rooted in traditional metallurgy. The superelasticity of Nickel-Titanium (NiTi) alloys was discovered in the 1960s [3], but it took 30 years to develop optimized products for replacing steel in stents. During this period, extensive research refined synthesis, precipitation, and heat treatment parameters [4]. Discussions on alloying effects, thermomechanical processing, precipitate sizes, and heat treatment conditions have resulted in over 10,000 publications and patents [4–12]. By 2015, NiTi held over 50% of the market share among metallic materials, with a market size of USD 33 billion. Despite its success, the reasons behind NiTi's outstanding performance remain unclear and irreproducible. The second largest group of shape memory alloys is Cu-based alloys, some of which exhibit higher superelastic strain than NiTi [13, 14]. However, the brittleness of polycrystalline Cu-based alloys limits their applications, especially under cyclic loading conditions [15, 16]. In single-crystalline form, both superelasticity and functional fatigue are orientation-dependent [17, 18]. Despite significant research efforts to improve their functional fatigue properties, the results have been unsatisfactory [11, 15, 16].

The mathematical design method has been effectively utilized to discover low-hysteresis shape memory alloys, which can be formally employed in their development. A notable example is the discovery of shape memory alloys with minimal hysteresis [19]. It has been demonstrated that satisfying the cofactor conditions [20] enables the formation of novel microstructures, significantly enhancing the phase transformation reversibility of the material [19, 21]. The cofactor conditions provide a mathematical foundation that facilitates the rationalization and minimization of experimental trials, thereby reducing thermal hysteresis and improving various functional fatigue properties in shape memory alloys.

Based on rigorous mathematical derivation and a systematic study of the structure-property relationships in the $Cu25Zn45Au_{30}$ alloy and its nearby compositions, we identified a unified descriptor for the microstructure-related properties of phase-transforming materials: the *transformation stretch tensor*. This tensor, which depends on lattice parameters, can be algorithmically determined using the StructTrans algorithm [22]. When the transformation stretch tensor satisfies the *mechanics criteria* (i.e., the cofactor conditions), the material exhibits significant enhancement in functional fatigue properties during cycles of both thermally driven [19] and stress-induced [21, 23, 24] phase transformations. This discovery provides a conceptual framework for designing shape memory alloys. However, the specific methods for optimizing individual alloy systems using this framework are still under investigation.

In this paper, we will exploit the synergy of the theories, the suite of algorithms, and the advanced characterizations for the development of Cu-based shape memory alloys with optimized functional fatigue properties. Here, the CuAlMn alloy system is chosen to explore the above aims. Depending on the composition, the phase transformation of this alloy system is complicated and interesting, that is from cubic (β

phase) to different martensite structures (*i.e.* 2H, 6M or 18R phases). By our approach, if we successfully optimize this alloy system, the design strategy can be transferred to develop other alloy systems. Eventually, we will enlarge the engineering applications of Cu-based alloys.

2. Theory of design based on kinematic compatibility conditions

2.1. Material descriptor

Based on numerous experimental and algorithmic studies [19, 20, 22, 25–27], the transformation stretch tensor is an n-variable tensor in $\mathbb{R}^{3\times3}$, where $n \leq 4$. For cubic to monoclinic transformations, $n = 4$; for cubic to orthorhombic transformations, $n = 3$; and for cubic to tetragonal transformations, $n = 2$. However, the stretch tensor does not explicitly define the tuning parameters for design. During alloy design, we adjust the compositions, which slightly modify the lattice parameters of austenite and martensite, thereby parameterizing the transformation stretch tensor. Although the StructTrans algorithm [22] provides the numerical expression of the transformation stretch tensor for a specific phase transformation, it does not offer an explicit analytical expression as a function of these tuning parameters.

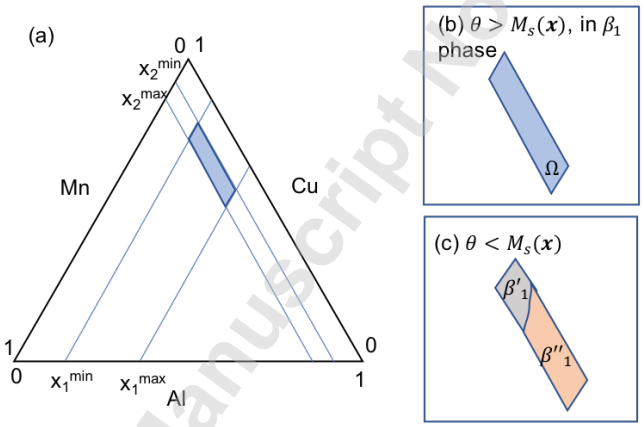

Figure 1: 2-dimensional composition space of Cu-Al-Mn alloy. (a) The selected domain of study, which is (b) in single phase of austenite (β_1) at temperature higher than M_s, while (c) separates into different phases of martensite at temperature lower than M_s.

In this section, we explore the tensor valued function $\mathbf{U} : \Omega \to \mathbb{R}^{3\times3}$ as a descriptor of the ternary CuAlMn for the two-parameter compositional domain $\Omega = [x_1^{\min}, x_1^{max}] \times [x_2^{min}, x_2^{max}]$. Figure 1 elaborates the compositional domain selected for investigation, bounded by Al composition varying between $x_1^{\min}$ and $x_1^{\max}$ and Mn composition varying between $x_2^{\min}$ and $x_2^{\max}$, depicted in Figure 1(a). According to the previous study of this system, the symmetry of the austenite in Ω (Figure 1b) is $Fm\bar{3}m$ [28], while the symmetry of the martensite is either monoclinic or orthorhombic, as seen in Figure 1(c). The orthorhombic symmetry can be seen as the deduction of monoclinic symmetry with the angle $\beta = 90°$. Assuming the monoclinic angle, $\beta \in [60°, 120°]$, we can define a mapping $\mathcal{LP} : \Omega \to \mathbb{R}^4_+ \times (-\frac{1}{2}, \frac{1}{2})$[1] to represent the variation of lattice

[1] $\mathbb{R}^4_+$ denotes a tuple of 4 strictly positive real numbers.

parameters on Ω. The lattice parameter mapping $\mathcal{LP}$ has five components

$$\mathcal{LP} = (p_0(\mathbf{x}), p_1(\mathbf{x}), p_2(\mathbf{x}), p_3(\mathbf{x}); c(\mathbf{x})) \text{ for all } \mathbf{x} \in \Omega. \tag{1}$$

where function p_0 denotes the lattice parameter of cubic austenite, functions p_i, $i = 1, 2, 3$ denotes the edge lengths of martensite unit cell, and c represents the cosine of the monoclinic angle. The transformation stretch tensor can be seen as a mapping from the image of the lattice parameter function defined in (1) for all compositional variable $\mathbf{x} \in \Omega$. The conventional lattice vectors of cubic austenite can be expressed as

$$\mathbf{E}_A(p_0) = p_0\mathbf{I} = \begin{bmatrix} p_0 & 0 & 0 \\ 0 & p_0 & 0 \\ 0 & 0 & p_0 \end{bmatrix}. \tag{2}$$

Here, it is clear that $\mathbf{E}_A$ is a linear function of p_0. Note that the expression of the conventional lattice vectors may be different from the primitive lattice vectors for complex lattices such as face-centered and body-centered cubic, body-centered tetragonal, base-centered monoclinic etc. In such cases, we can use a re-base transformation [28] to relate the expressions of conventional and primitive lattice basis vectors, which can be carried along with the transformation stretch tensor calculations. To unify the presentation basis, the normalized cubic basis vectors, $\mathbf{e}_1 = (1, 0, 0)$, $\mathbf{e}_2 = (0, 1, 0)$, and $\mathbf{e}_3 = (0, 0, 1)$ are used to express the lattice vectors of the low-symmetry phase deformed from cubic austenite. During phase transformations from cubic austenite, the martensite may possess a simple lattice or complex lattices. If the phase transformation results in a simple lattice, the primitive lattice vectors of martensite can be written as

$$\mathbf{E}_M(p_1, p_2, p_3; c) = p_1\mathbf{e}_1 \otimes \mathbf{e}_1 + p_2\mathbf{e}_2 \otimes \mathbf{e}_2 + p_3\sqrt{1-c^2}\mathbf{e}_3 \otimes \mathbf{e}_3 + p_3 c\mathbf{e}_1 \otimes \mathbf{e}_3, \tag{3}$$

in terms of four variables $(p_1, p_2, p_3; c) \in \mathbb{R}^3_+ \times (-\frac{1}{2}, \frac{1}{2})$. The variants of martensite can be derived from the symmetry operations [29, 30]. If the martensite phase is a complex lattice, e.g. base-centered monoclinic, we can convert the primitive basis to the conventional basis by re-base transformation. According to Cauchy-Born rule [31–33], there exists a set of lattice correspondences given by $\mathbf{L} \in \mathbb{R}^{3\times3}$ defined in reference [22], such that

$$\mathbf{U}^2 = (\mathbf{E}_A\mathbf{L})^{-T}\mathbf{E}_M^T\mathbf{E}_M(\mathbf{E}_A\mathbf{L})^{-1}. \tag{4}$$

Substituting the equations (2) and (3) into (4) and taking the square root, we get the expression of material descriptor

$$\mathbf{U} = \frac{1}{p_0}\sqrt{\mathbf{C}_p}, \tag{5}$$

where $\mathbf{C}_p = (\mathbf{L})^{-T}\mathbf{E}_M^T\mathbf{E}_M(\mathbf{L})^{-1}$. Here the square root means the polar decomposition of matrix $\mathbf{C}_p$.

By observation, the material descriptor $\mathbf{U}$ given by (5) is positive definite and symmetric. The expression (5) also implies that among five lattice parameter variables $(p_0, p_1, p_2, p_3; c)$, the transformation stretch tensor

only depends on 4 independent variables as the austenite lattice parameter p_0 acts as a scaling factor that modulates the stretch tensor. The derivatives of $\mathbf{U}$ with respective to lattice parameter $\mathcal{LP} \in \mathbb{R}^4_+ \times (-\frac{1}{2}, \frac{1}{2})$ are calculated as

$$\frac{\partial \mathbf{U}}{\partial p_0} = -\frac{1}{p_0^2}\sqrt{\mathbf{C}_p}, \tag{6}$$

$$\frac{\partial \mathbf{U}}{\partial p_1} = (\mathbf{L}^T\mathbf{U})^{-1}(\frac{p_1}{p_0}\mathbf{e}_1 \otimes \mathbf{e}_1 + \frac{p_3 c}{2p_0}\mathbf{e}_1 \otimes \mathbf{e}_3)(\mathbf{L})^{-1}, \tag{7}$$

$$\frac{\partial \mathbf{U}}{\partial p_2} = \frac{p_2}{p_0}(\mathbf{L}^T\mathbf{U})^{-1}(\mathbf{e}_2 \otimes \mathbf{e}_2)(\mathbf{L})^{-1}, \tag{8}$$

$$\frac{\partial \mathbf{U}}{\partial p_3} = (\mathbf{L}^T\mathbf{U})^{-1}(\frac{p_3}{p_0}\mathbf{e}_3 \otimes \mathbf{e}_3 + \frac{p_1 c}{2p_0}(\mathbf{e}_1 \otimes \mathbf{e}_3 + \mathbf{e}_3 \otimes \mathbf{e}_1))(\mathbf{L})^{-1}, \tag{9}$$

$$\frac{\partial \mathbf{U}}{\partial c} = \frac{p_1 p_3}{2p_0}(\mathbf{L}^T\mathbf{U})^{-1}(\mathbf{e}_1 \otimes \mathbf{e}_3 + \mathbf{e}_3 \otimes \mathbf{e}_1)(\mathbf{L})^{-1}. \tag{10}$$

The functions (5) to (10) are smooth in $\mathbb{R}^4_+ \times \left(-\frac{1}{2}, \frac{1}{2}\right)$. Previous X-ray diffraction studies [28] have shown that p_0 is continuous on Ω, indicating that the compositional domain is in the β_1 phase [34] when the temperature is higher than the transformation temperature θ_c. When the temperature is lower than the transformation temperature, discontinuities may exist in the selected compositional domain. In such cases, the compositional domain can be treated as a union of disjoint sub-domains with homogeneous lattice symmetries.

In this work, we synthesized alloys in the neighborhood of $\mathrm{CuAl}_{x_1}\mathrm{Mn}_{x_2}$ with Al compositions varying from 17 to 22 atomic % and Mn compositions varying from 9 to 11 atomic %. We determined the crystal structures and refined the lattice parameters for the austenite and martensite phases using synchrotron X-ray diffraction at the Advanced Light Source, Lawrence Berkeley National Lab. It was revealed that the continuity of the lattice parameters $(p_1, p_2, p_3; c)$ holds on the subdomain $[17, 22] \times [9, 11]$ atomic %.

2.2. Index function of compatibility

We have theorized the mechanics criteria as functions of the material descriptor. They are the cofactor conditions:

$$\lambda_2(\mathbf{U}) - 1 = 0, \tag{C-1}$$

$$\mathbf{a}(\mathbf{U}) \cdot \mathbf{U}\mathrm{cof}(\mathbf{U}^2 - \mathbf{I})\mathbf{n}(\mathbf{U}) = 0, \tag{C-2}$$

$$\mathrm{tr}\mathbf{U}^2 + \det \mathbf{U}^2 - (1/4)|\mathbf{a}(\mathbf{U})|^2|\mathbf{n}(\mathbf{U})|^2 \leq 2, \tag{C-3}$$

where λ_2 is the middle eigenvalue of the descriptor tensor, and the vectors $\mathbf{n}$ and $\mathbf{a}$ are the twinning parameters in terms of the 2-fold crystallographic axis $\mathbf{e}$ of austenite lattice, where

$$\text{Type I:} \quad \mathbf{n}_I = \mathbf{e}, \quad \mathbf{a}_I = 2(\frac{\mathbf{U}^{-1}\mathbf{e}}{|\mathbf{U}^{-1}\mathbf{e}|^2} - \mathbf{U}\mathbf{e})$$

$$\text{Type II:} \ \mathbf{n}_{II} = 2(\mathbf{e} - \frac{\mathbf{U}^2\mathbf{e}}{|\mathbf{U}\mathbf{e}|^2}), \quad \mathbf{a}_{II} = \mathbf{U}\mathbf{e}.$$

The reference [20] provides a rigorous theory for the formation of compatible microstructures in materials undergoing structural transformation when the transformation stretch tenor $\mathbf{U}$ satisfies (C-1), (C-2) and (C-3). A lot of experimental works [19, 21, 23, 25, 26, 35, 36] conclusively verify the dependence of the functional fatigue properties of phase-transforming materials on (C-1), (C-2) and (C-3).

Mathematically, the (C-1) condition underlies the energy barrier and the corresponding thermal hysteresis in martensitic phase transformation [35], while the (C-2) condition allows for the existence of infinitely many compatible austenite/martensite interfaces during phase transformation, which will accommodate intrinsic non-transforming defects and boundary conditions in material [20]. The inequality (C-3) is a mild condition that is always true for Type I and Type II twins when the first two conditions are closely satisfied. Note that (C-3) needs to be checked when considering the compatibility of the Compound twins. The contributions of the sub-conditions to the material properties are different. For example, the material thermal hysteresis and stress-free functional fatigue are mainly governed by (C-1), while the stress-induced (especially for demanding loading conditions) functionalities of polycrystalline solids strongly depend on the satisfaction of (C-2).

Based on the cofactor conditions (C-1) and (C-2), here we propose to study mathematically the following indexer functions:

$$f(\mathbf{U}) = \lambda_2 - 1 \tag{CP-1}$$

$$g(\mathbf{U}) = (\lambda_2 - 1)^2 + (|\mathbf{U}^{-1}\mathbf{e}| - 1)^2 + (|\mathbf{U}\mathbf{e}| - 1)^2 \tag{CP-2}$$

$$h(\mathbf{U}) = (\lambda_2 - 1)^2 + |\mathbf{e} \cdot \mathbf{v}_2|(1 - \frac{\lambda_2^2}{|\mathbf{U}\mathbf{e}|^2})^2. \tag{CP-3}$$

Here, the $\mathbf{v}_2$ is the eigenvector of $\mathbf{U}$ associated with the middle eigenvalue λ_2. In Figure 1, we have defined the compositional domain Ω where the lattice parameters continuously vary with respect to compositions. The Eq. (5) shows that the descriptor $\mathbf{U}$ is a continuous function of lattice parameters, thus finding the optimal compositions is equivalent to numerically seeking the root of $f = 0$, $g = 0$ or $h = 0$. The root of $f = 0$ indicates that the middle principal stretch of the phase transformation is unity, which significantly influences the thermal hysteresis of shape memory alloys [26, 27, 35]. The equation $g = 0$ ensures that the alloy satisfies the cofactor conditions for both Type I and Type II twins, while the equation $h = 0$ ensures satisfaction of the cofactor conditions for Compound twins. The root property and the analytical gradient expressions of the indexer functions indicate the tuning direction to achieve the satisfaction of the compatibility conditions.

2.3. Gradient of λ_2

Consider any 4-variable positive definite symmetry tensor written in an orthogonal basis

$$\mathbf{U} = \begin{bmatrix} \alpha & \beta & 0 \\ \beta & \delta & 0 \\ 0 & 0 & \gamma \end{bmatrix}, \tag{11}$$

where $\alpha, \beta, \gamma \in (0, \infty)$ and $\beta \in \mathbb{R}$. When $\alpha = \delta$, $\mathbf{U}$ represents a cubic to orthorhombic phase transformation; When $\beta = 0$ and $\alpha = \delta$, $\mathbf{U}$ represents a cubic to tetragonal phase transformation; Otherwise $\mathbf{U}$ presents a cubic to monoclinic phase transformation. We need to be careful that there are two ways of writing the stretch tensors for cubic to monoclinic transformations: one is given in Eq. (11), the other one can be derived by $\mathbf{RUR}^T$ for the rotation matrix $\mathbf{R}_{\mathbf{w}}^{\frac{\pi}{2}} \in SO(3)$. Here $\mathbf{w} = (-1, -1, 0)$ represents the rotational axis. The superscript $\frac{\pi}{2}$ denotes the angle of rotation about the axis $\mathbf{w}$. Therefore, the matrix presentation in Eq. (11) can be generally used for describing the phase-transforming materials from cubic-type austenite to at least monoclinic martensite.

The three eigenvalues of $\mathbf{U}$ are γ, $\frac{1}{2}(\alpha + \delta - s)$ and $\frac{1}{2}(\alpha + \delta + s)$ where $s = \sqrt{\alpha^2 + 4\beta^2 - 2\alpha\delta + \delta^2}$ corresponding to the eigenvectors $(0, 0, 1)$, $(\alpha - \delta - s, 2\beta, 0)$ and $(\alpha - \delta + s, 2\beta, 0)$. If the inequality $\beta^2 > (\gamma - \alpha)(\gamma - \delta)$ holds, the middle eigenvalue is trivial, i.e. $\lambda_2 = \gamma$ corresponding to the eigenvector $(0, 0, 1)$. However, this is not common for phase-transforming shape memory alloys, especially in Cu-based alloys [13, 16, 20, 22, 37]. Here we present two non-trivial cases under the constraint $\beta^2 < (\gamma - \alpha)(\gamma - \delta)$:

Case 1: If $0 < \gamma < \delta$, $\lambda_2 = \frac{1}{2}(\alpha + \delta - s)$. The gradient of λ_2 with respect to $\mathbf{U}$ is

$$(\nabla\lambda_2)_1 = \frac{\partial\lambda_2}{\partial\mathbf{U}} = \begin{bmatrix} \frac{1}{2}(1 - \frac{\alpha-\delta}{s}) & -\frac{2\beta}{s} & 0 \\ -\frac{2\beta}{s} & \frac{1}{2}(1 + \frac{\alpha-\delta}{s}) & 0 \\ 0 & 0 & 0 \end{bmatrix} \tag{12}$$

Case 2: If $\gamma > \delta + 2\beta^2 > 0$, $\lambda_2 = \frac{1}{2}(\alpha + \delta + s)$. The gradient of λ_2 with respect to $\mathbf{U}$ is

$$(\nabla\lambda_2)_2 = \frac{\partial\lambda_2}{\partial\mathbf{U}} = \begin{bmatrix} \frac{1}{2}(1 + \frac{\alpha-\delta}{s}) & \frac{2\beta}{s} & 0 \\ \frac{2\beta}{s} & \frac{1}{2}(1 - \frac{\alpha-\delta}{s}) & 0 \\ 0 & 0 & 0 \end{bmatrix} = \mathbf{Q}(\nabla\lambda_2)_1\mathbf{Q}^T, \tag{13}$$

for a rotation matrix $\mathbf{Q} \in SO(3)$ about the rotational axis $(0, 0, 1)$ for an angle of $\frac{\pi}{2}$.

2.4. Tuning directions

The compositional tuning can be analytically and explicitly guided by the kinematic compatibility conditions given in (CP-1), (CP-2), and (CP-3). These conditions should be tailored to achieve the desired roots, which are evaluated using the indexer function and its numerical gradient. For developing polycrystalline

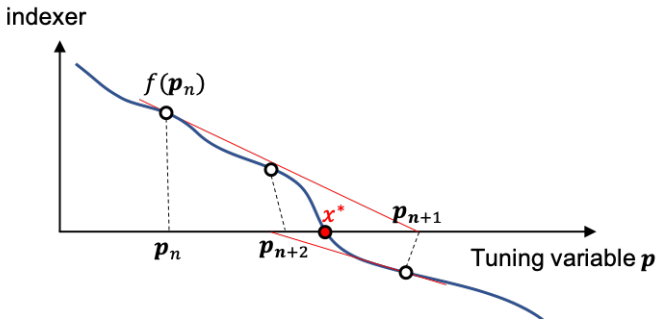

Figure 2: Schematic illustration of the tuning algorithm according to the indexer function.

Cu-based β alloys, we start with the indexer function $f = \lambda_2 - 1$. Figure 2 illustrates our alloy development strategy. The core idea is to experimentally apply the Newton-Raphson numerical algorithm to identify the lattice parameters that satisfy the mechanics criterion $f = 0$.

Suppose we have conducted the nth experiment with the composition variable $\mathbf{x}_n \in \Omega$, the lattice parameters $\mathbf{p}_n = \mathcal{LP}(\mathbf{x}_n) \in \mathbb{R}^4 \times (-\frac{1}{2}, \frac{1}{2})$. Experimentally, the lattice parameter mapping $\mathcal{LP}$ can be established by a series of X-ray diffraction measurements. Then the Eq. (5) directly calculates the value of $f_n = f(\mathbf{p}_n)$ with a determined lattice correspondence matrix. The Jacobian of the indexer function can be directly expressed by Eqs. (6) - (10) and (12) in indicial notation as

$$f'_n = \left(\frac{\partial f}{\partial \mathbf{p}}\right)_{\mathbf{p}_n} = \left(\frac{\partial \lambda_2}{\partial \mathbf{U}_{ij}} \cdot \frac{\partial \mathbf{U}_{ij}}{\partial p_k}\right)_{\mathbf{p}_n}. \tag{14}$$

Then the next target lattice parameters $\mathbf{p}_{n+1}$ can be derived by solving

$$f'_n \cdot \mathbf{p}_{n+1} = f'_n \cdot \mathbf{p}_n - f_n. \tag{15}$$

Using the Jacobian (14) and Newton's iterative algorithm given by Eq. (15), we can effectively identify the tuning direction based on the existing compositions along the descent of the gradient of the indexer function.

3. Functionality of designed Cu-based alloys

To validate our rational design strategy, we conducted experiments on three distinct Cu-based alloys with nominal atomic compositions of $\mathrm{CuAl}_{x_1}\mathrm{Mn}_{x_2}$, where $(x_1, x_2) \in [0.17, 0.22] \times [0.09, 0.11]$. Table 1 summarizes the values of f_n, f'_n, and $|f'_n|$ for these alloy compositions. Notably, $\mathrm{CuAl}_{17.2}\mathrm{Mn}_{10.3}$ composition yields $f'_n(i,j) = (-0.00084, 0.02004)$, indicating an increasing direction for x_1 and decreasing direction for x_2. Consequently, we synthesized the $\mathrm{CuAl}_{21.5}\mathrm{Mn}_{9.5}$ composition with elevated x_1 and reduced x_2 values. The calculated $f'_n(i,j) = (0.00691, -0.01919)$ indicated that the next tuning direction should be towards lower x_1 and higher x_2 values. The composition $\mathrm{CuAl}_{19.6}\mathrm{Mn}_{10.8}$, fabricated along this tuning direction, yields a much smaller $|f'_n| = 0.006819$. The proximity of this value to zero, along with the negative components of $f'_n(i,j)$, led us to the final composition of $\mathrm{CuAl}_{20.2}\mathrm{Mn}_{11.3}$ with slightly increased Al and Mn contents.

Table 1: Calculated values of f_n, f'_n, and $|f'_n|$ for three alloy compositions

Compositions (at.%) of a ternary alloy $CuAl_{x_1}Mn_{x_2}$		f_n	f'_n	$\lvert f'_n \rvert$
x_1	x_2			
17.2	10.3	0.011910	$(-0.00084, 0.02004)$	0.020056
21.5	9.5	0.011661	$(0.00691, -0.01919)$	0.020396
19.6	10.8	0.007952	$(-0.00591, -0.0034)$	0.006819

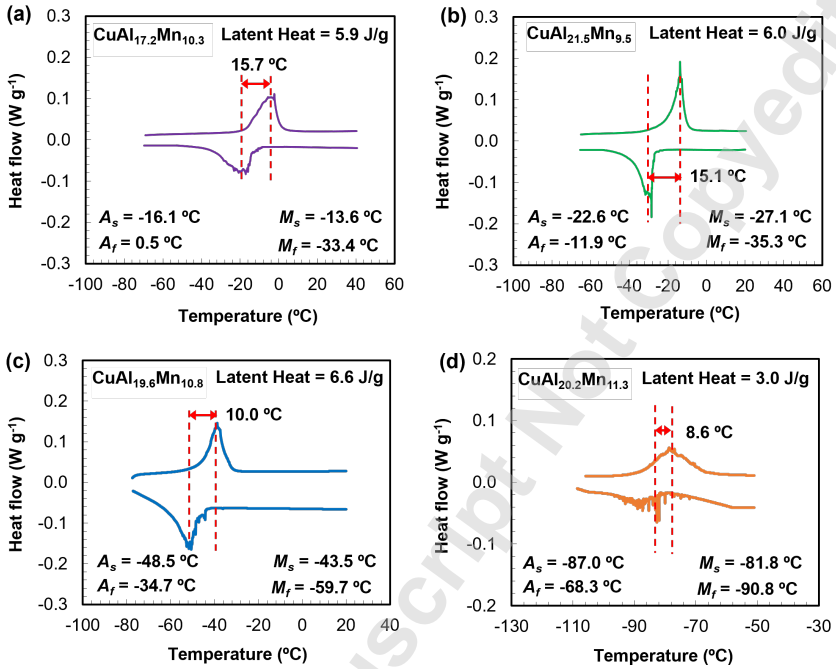

Figure 3: DSC analysis during a thermally driven phase transformation for (a) $CuAl_{17.2}Mn_{10.3}$, (b) $CuAl_{21.5}Mn_{9.5}$, (c) $CuAl_{19.6}Mn_{10.8}$, and (d) $CuAl_{20.2}Mn_{11.3}$.

To examine the thermal functionality of these Cu-based compositions, we utilized differential scanning calorimetry (TA Instruments DSC250). Figure 3 illustrates the DSC analysis of the four synthesized compositions during a thermally driven phase transformation. It highlights the transformation temperatures and thermal hysteresis in the alloys as they undergo a complete phase transformation from martensite to austenite and then back to martensite. The austenite start/finish (A_s/A_f) and martensite start/finish (M_s/M_f) temperatures were identified as the onset of heat absorption/emission peaks. The thermal hysteresis was determined as $\Delta T = \frac{1}{2}(A_s + A_f - M_s - M_f)$. Transformation temperatures, latent heat, and thermal hysteresis values for the four compositions are summarized in Figure 3(a)-(d). Comparing the thermal hysteresis displayed in Figure 3(a)-(c) with the $|f'_n|$ values in Table 1 reveals a direct correlation. Compositions with lower $|f'_n|$ values exhibit reduced hysteresis, aligning with our theoretical framework. Remarkably, through only three iterations, the thermal hysteresis was reduced by a factor of 2, demonstrating the effectiveness of

our tuning strategy. As anticipated, the optimally designed $CuAl_{20.2}Mn_{11.3}$ composition demonstrates the least hysteresis among all compositions.

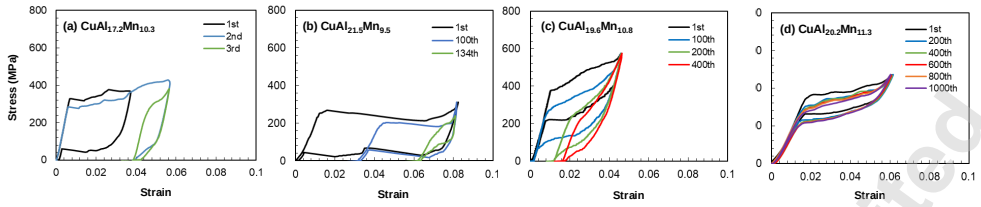

Figure 4: The true stress–strain responses at various number of cycles for the micropillars of (a) $CuAl_{17.2}Mn_{10.3}$, (b) $CuAl_{21.5}Mn_{9.5}$, (c) $CuAl_{19.6}Mn_{10.8}$, and (d) $CuAl_{20.2}Mn_{11.3}$ compositions.

To delve deeper into the reversibility of the alloys under stress-induced phase transformation, we performed microcompression cycling tests on the fabricated single-crystal pillars with a fixed loading rate of 200 μN/s at room temperature using Hysitron TI980 TriboIndenter. During each stress-induced transformation cycle, the pillar underwent loading until the phase transformation from austenite to martensite was completed, followed by a full unloading to restore the superelastic deformation. The specifics of pillar fabrication and microcompression testing procedures are detailed elsewhere [17]. Figure 4 depicts the true stress–strain curves from the microcompression tests on the $\sim 2\mu$m-diameter pillars of three different compositions at varying numbers of cycles. The superelastic behavior is evident across all compositions, albeit with a gradual decline in functionality as the number of cycles increases. This decline is particularly pronounced in the $CuAl_{21.5}Mn_{9.5}$ and $CuAl_{19.6}Mn_{10.8}$ pillars, which lose their functionalities after 134 and 400 cycles, respectively, as depicted in Figure 4(a) and (b). In contrast, the pillar composed of $CuAl_{20.2}Mn_{11.3}$ maintains functionality even after 1000 cycles, with a retained 6% recoverable strain (Figure 4(c)). This suggests a substantial enhancement in the functional stability of the optimized composition, highlighting the reliability of our theoretical approach in predicting compositions with superior reversibility. The scanning electron microscopy (SEM) images of the pillars of varying compositions before and after cyclic loading are shown in Figure 5. The presence of permanent deformations in the form of shortening is noticeable in the first three compositions (Figure 5(a-c)). However, the pillar with the optimal composition does not exhibit this shortening phenomenon; instead, only localized deformation traces are visible on the lateral surface of the pillar that do not yield the residual strain, as shown in Figure 5(d).

4. Conclusions

In summary, we leveraged the harmonious interplay between theoretical frameworks, an array of algorithms, and sophisticated characterizations to advance the development of Cu-based shape memory alloys with heightened functional fatigue properties. The theoretical methodology was illustrated using a series of $CuAl_{x_1}Mn_{x_2}$ alloys, with Al compositions varying from 17 to 22 atomic % and Mn compositions varying

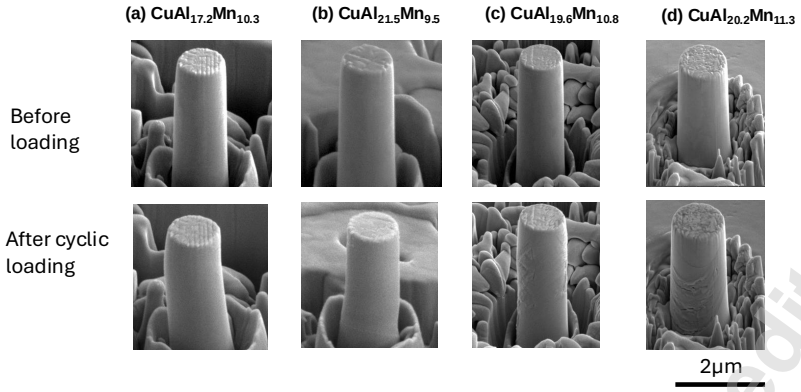

Figure 5: The SEM images of micropillars before and after cyclic loading for (a) $CuAl_{17.2}Mn_{10.3}$, (b) $CuAl_{21.5}Mn_{9.5}$, (c) $CuAl_{19.6}Mn_{10.8}$, and (d) $CuAl_{20.2}Mn_{11.3}$ compositions.

from 9 to 11 atomic %. By utilizing a scalar-valued function to map the functional fatigue property based on cofactor conditions, we explored the continuity and extremes concerning compositional variables. With just three iterative refinement steps, we pinpoint the $CuAl_{20.2}Mn_{11.3}$ composition, resulting in a halving of the thermal hysteresis and bolstering mechanical reversibility for up to 1000 cycles. This underscores the efficacy of mathematical methodologies as expedient tools for material development with exceptional properties.

Acknowledgements

M. K. and X. C. thank the financial support of the HK Research Grants Council under Grant No. 16203021, 16204022 and No. 16203023. M. K. thanks the financial support of the Sharif University of Technology Research Grant Council under Grant No. G4030310. Advanced Light Source was supported by the Office of Science, Office of Basic Energy Sciences, of the U.S. Department of Energy under Contract No. DE-AC02-05CH11231.

References

[1] E. Warburg, Magnetische untersuchungen, Annalen der Physik 249 (5) (1881) 141–164.
[2] R. A. Millikan, A direct photoelectric determination of Planck's" h", Physical Review 7 (3) (1916) 355.
[3] W. J. Buehler, J. Gilfrich, R. Wiley, Effect of low-temperature phase changes on the mechanical properties of alloys near composition tini, Journal of applied physics 34 (5) (1963) 1475–1477.
[4] K. Otsuka, X. Ren, Physical metallurgy of Ti–Ni-based shape memory alloys, Progress in materials science 50 (5) (2005) 511–678.
[5] D. Abujudom, P. Thoma, S. Fariabi, The effect of cold work and heat treatment on the phase transformations of near equiatomic niti shape memory alloy, in: Materials Science Forum, Vol. 56, Trans Tech Publ, 1990, pp. 565–570.
[6] K. Yeung, K. Cheung, W. Lu, C. Chung, Optimization of thermal treatment parameters to alter austenitic phase transition temperature of NiTi alloy for medical implant, Materials Science and Engineering: A 383 (2) (2004) 213–218.
[7] C. P. Frick, A. M. Ortega, J. Tyber, A. E. M. Maksound, H. J. Maier, Y. Liu, K. Gall, Thermal processing of polycrystalline NiTi shape memory alloys, Materials Science and Engineering: A 405 (1-2) (2005) 34–49.
[8] K. Gall, J. Tyber, G. Wilkesanders, S. W. Robertson, R. O. Ritchie, H. J. Maier, Effect of microstructure on the fatigue of hot-rolled and cold-drawn NiTi shape memory alloys, Materials Science and Engineering: A 486 (1-2) (2008) 389–403.
[9] E. Pereira, I. Peixoto, A. Viana, I. Oliveira, B. Gonzalez, V. Buono, M. Bahia, Physical and mechanical properties of a thermomechanically treated NiTi wire used in the manufacture of rotary endodontic instruments, International Endodontic Journal 45 (5) (2012) 469–474.
[10] M. H. Elahinia, M. Hashemi, M. Tabesh, S. B. Bhaduri, Manufacturing and processing of NiTi implants: A review, Progress in materials science 57 (5) (2012) 911–946.
[11] T. W. Duerig, K. Melton, D. Stöckel, Engineering aspects of shape memory alloys, Butterworth-Heinemann, 2013.
[12] S. Saedi, A. S. Turabi, M. T. Andani, C. Haberland, H. Karaca, M. Elahinia, The influence of heat treatment on the thermomechanical response of Ni-rich NiTi alloys manufactured by selective laser melting, Journal of Alloys and Compounds 677 (2016) 204–210.
[13] K. Otsuka, C. Wayman, K. Nakai, H. Sakamoto, K. Shimizu, Superelasticity effects and stress-induced martensitic transformations in CuAlNi alloys, Acta Metallurgica 24 (3) (1976) 207 – 226.
[14] J. Dutkiewicz, H. Kato, S. Miura, U. Messerschmidt, M. Bartsch, Structure changes during pseudoelastic deformation of cualmn single crystals, Acta Materialia 44 (11) (1996) 4597 – 4609.
[15] S. Miyazaki, K. Otsuka, Development of shape memory alloys, Isij International 29 (5) (1989) 353–377.
[16] T. Tadaki, Cu-based shape memory alloys, Shape memory materials (1998) 97–116.
[17] M. Karami, Z. Zhu, Z. Zeng, N. Tamura, Y. Yang, X. Chen, Two-tier compatibility of superelastic bicrystal micropillar at grain boundary, Nano letters 20 (11) (2020) 8332–8338.
[18] M. Karami, K. Chu, Z. Zhu, Z. Wang, Q. Sun, M. Huang, X. Chen, Orientation-dependent superelasticity and fatigue of cualmn alloy under in situ micromechanical tensile characterization, Journal of the Mechanics and Physics of Solids 160 (2022) 104787.
[19] Y. Song, X. Chen, V. Dabade, T. W. Shield, R. D. James, Enhanced reversibility and unusual microstructure of a phase-transforming material, Nature 502 (2013) 85.
[20] X. Chen, V. Srivastava, V. Dabade, R. D. James, Study of the cofactor conditions: conditions of supercompatibility between phases, J. Mech. Phys. Solids 61 (2013) 2566.
[21] C. Chluba, W. Ge, R. Lima de Miranda, J. Strobel, L. Kienle, E. Quandt, M. Wuttig, Ultralow-fatigue shape memory alloy films, Science 348 (6238) (2015) 1004.
[22] X. Chen, Y. Song, N. Tamura, R. D. James, Determination of the stretch tensor for structural transformation, J. Mech. Phys. Solids 93 (2016) 34–43.
[23] X. Ni, J. R. Greer, K. Bhattacharya, R. D. James, X. Chen, Exceptional Resilience of Small-Scale $Au_{30}Cu_{25}Zn_{45}$ under Cyclic Stress-Induced Phase Transformation, Nano Letters (2016).
[24] M. Karami, Z. Zhu, K. H. Chan, P. Hua, N. Tamura, X. Chen, Nondissipative martensitic phase transformation after multimillion superelastic cycles, Physical Review Letters 132 (6) (2024) 066101.
[25] V. Srivastava, X. Chen, R. D. James, Hysteresis and unusual magnetic properties in the singular Heusler alloy $Ni_{45}Co_5Mn_{40}Sn_{10}$, Applied Physics Letters 97 (1) (2010) 014101.
[26] R. Zarnetta et al., Identification of Quaternary Shape Memory Alloys with Near-Zero Thermal Hysteresis and Unprecedented Functional Stability, Advanced Functional Materials 20 (12) (2010) 1917–1923.
[27] J. Cui, Y. S. Chu, O. O. Famodu, Y. Furuya, J. Hattrick-Simpers, R. D. James, A. Ludwig, S. Thienhaus, M. Wuttig, Z. Zhang, et al., Combinatorial search of thermoelastic shape-memory alloys with extremely small hysteresis width, Nature materials 5 (4) (2006) 286.
[28] M. Karami, N. Tamura, Y. Yang, X. Chen, Derived crystal structure of martensitic materials by solid–solid phase transformation, Acta Crystallographica Section A: Foundations and Advances 76 (4) (2020) 521–533.
[29] J. M. Ball, R. D. James, Fine phase mixtures as minimizers of energy, Archive for Rational Mechanics and Analysis 100 (1987) 13–52.
[30] J. M. Ball, R. D. James, Proposed experimental tests of a theory of fine microstructure and the two-well problem, Philosophical Transactions of the Royal Society of London. Series A: Physical and Engineering Sciences 338 (1650) (1992) 389–450.
[31] J. Ericksen, Some phase transitions in crystals, Archive for Rational Mechanics and Analysis 73 (1980) 99–124.
[32] J. Ericksen, Weak martensitic transformations in bravais lattices, in: Mechanics and Thermodynamics of Continua: A Collection of Papers Dedicated to BD Coleman on His Sixtieth Birthday, Springer, 1991, pp. 145–158.

[33] J. Ericksen, The cauchy and born hypotheses for crystals, Mechanics and mathematics of crystals: selected papers of JL Ericksen 117 (2005).
[34] K. Otsuka, H. Sakamoto, K. Shimizu, Successive stress-induced martensitic transformations and associated transformation pseudoelasticity in Cu–Al–Ni alloys, Acta Metallurgica 27 (1979) 585–601.
[35] Z. Zhang, R. D. James, S. Müller, Energy barriers and hysteresis in martensitic phase transformations, Acta Materialia 57 (15) (2009) 4332 – 4352.
[36] J. Liu, T. Gottschall, K. P. Skokov, J. D., M. O. Gutfleisch, Giant magnetocaloric effect driven by structural transitions, Nature Mater. 11 (7) (2012) 620–626.
[37] L. Chang, T. Read, Behavior of the elastic properties of aucd, Trans Met Soc AIME 191 (1951) 47.